

# Fluorescence Imaging *In Vivo* up to 1700 nm

Shuo Diao<sup>1,4</sup>, Jeffrey L. Blackburn<sup>2,4</sup>, Guosong Hong<sup>1,4</sup>, Alexander L. Antaris<sup>1</sup>, Junlei Chang<sup>3</sup>, Justin Z. Wu<sup>1</sup>, Bo Zhang<sup>1</sup>, Calvin J. Kuo<sup>3</sup> and Hongjie Dai<sup>1,\*</sup>

1. Department of Chemistry, Stanford University, Stanford, California 94305, USA.
2. Chemical and Materials Science Center, National Renewable Energy Laboratory, 1617 Cole Boulevard, Golden, Colorado 80401, USA.
3. Division of Hematology, School of Medicine, Stanford University, Stanford, California 94305, USA.
4. These authors contribute to the work equally

\* Correspondence should be addressed to: [hdai@stanford.edu](mailto:hdai@stanford.edu)

## Abstract:

**Compared to visible and near-infrared regions below ~ 900 nm, imaging in the second near-infrared window beyond 1000 nm (NIR-II, 1000-1700 nm) is promising for deep-tissue high-resolution optical imaging *in vivo* owing to reduced scattering of photons traversing through tissues. Here, we succeeded fluorescence imaging *in vivo* in the long 1500-1700 nm (NIR-IIb) region using a novel, chemical separation enriched large-diameter semiconducting single-walled carbon nanotube material. Imaging in the 1500-1700 nm window resolved 3-4  $\mu$ m wide capillary blood vessels at ~ 3 millimeters depth through the intact body and brain of mice with the ability of blood-flow speed mapping in individual capillary vessels. Further, non-invasive single fluorophore imaging inside the tumor of a live mouse was achieved in the 1500-1700 nm window. NIR-IIb imaging can be generalized to a wide range of fluorophores emitting up to 1700 nm for a new paradigm of high performance *in vivo* optical imaging.**

Fluorescence-based optical imaging is indispensable to investigating biological systems with high spatial resolution and fast temporal speed.<sup>[1]</sup> However, a formidable challenge to *in vivo* fluorescence imaging of live animals has been the limited depth of penetration and inability of high resolution imaging through live tissues due to both absorption and scattering of photons. To circumvent this problem, we and others have recently explored *in vivo* fluorescence imaging

in the so called second near-infrared (NIR-II, 1000-1700 nm) window to benefit from reduced photon scattering and achieve higher imaging resolution deeper in the body than traditional NIR imaging.<sup>[2]</sup> Nevertheless, NIR-II fluorophores used thus far mainly emit below ~1400 nm, still non-optimal from the tissue scattering point of view. Although *in vivo* fluorescence imaging at longer wavelengths would further reduce scattering, increased water absorption approaching the infrared region could diminish light intensity through biological tissues, which is a valid concern that has deterred fluorescence imaging *in vivo* in the long NIR region. Another consideration for the development of *in vivo* fluorescence imaging in the long NIR window is the lack of biocompatible emitters with sufficient brightness. To date, most NIR-II *in vivo* fluorescence imaging has utilized high-pressure carbon monoxide conversion (HiPCO) SWNTs with a small diameter distribution of 0.7-1.1 nm, emitting band-gap fluorescence in the range of 1000-1400 nm.<sup>[2b, 2g-i, 2l, 3]</sup> We expect that SWNTs with larger diameters, such as SWNTs grown by laser vaporization method originally developed by Smalley,<sup>[4]</sup> could enable high-resolution fluorescence imaging in the longer wavelength region. However, the trend of lower fluorescence quantum yield for larger SWNTs makes it uncertain if large SWNTs grown by laser vaporization are bright enough for *in vivo* fluorescence imaging.<sup>[5]</sup>

We postulate that the long NIR-II 1500-1700 nm region offers a balance of photon scattering and water absorption effects, promising to afford optimal performance of fluorescence imaging *in vivo* to achieve both optimal penetration depth and imaging resolution. As shown in the absorption spectra of water and biological tissues (Fig. 1a), the 1500-1700 nm region resides in a local valley between a water vibrational OH-stretching overtone absorption peak at ~ 1450 nm and the edge of an increasing water absorption combination band beyond 1700 nm. Thus, the near ~ 1700 nm fluorescence imaging window offers a local minimum in the water absorption spectrum to minimize attenuation of fluorescence signal caused by water dominant in biological tissues. On the other hand, since scattering of photons scales as  $\lambda^{-\alpha}$  ( $\alpha = 0.2-4$  for different tissues),<sup>[6]</sup> the 1500-1700 nm window provides the lowest photon scattering in the entire near infrared window useful for high-resolution, deep-tissue biological imaging.

This work reports successful *in vivo* fluorescence imaging (under 808 nm excitation) in the 1500-1700 nm NIR-II window (named ‘NIR-IIb’ window), enabled by chemically enriching semiconducting laser vaporization SWNTs with much improved fluorescence brightness over unsorted SWNTs. The NIR-IIb imaging window affords an unprecedented *in vivo* vascular

imaging spatial resolution of 3-4  $\mu$ m at a depth of up to  $\sim$  3 millimeters in the mouse hindlimb and brain with intact skull and scalp. Single-vessel resolved blood flow speed mapping simultaneously for multiple hindlimb arterial vessels is also achieved based on video-rate fluorescence imaging in NIR-IIb region. Moreover, owing to high signal-to-background ratios, NIR-IIb fluorescence imaging allows for the first non-invasive single fluorophore imaging in live mice in the  $> 1000$  nm window. It is important to note that the high performance NIR-IIb imaging demonstrated here with nanotubes can be generalized to any other classes of fluorescent agents emitting near 1700 nm.

The SWNT NIR-IIb emitters with a diameter range of 0.96-1.24 nm were synthesized by laser vaporization (LV).<sup>[7]</sup> Changing the furnace temperature employed during LV synthesis from 950 °C to 1125 °C tuned the SWNT diameter distribution from  $\sim$ 0.8 to  $\sim$ 1.4 nm, allowing us to identify the brightest SWNTs grown at 950 °C for imaging in the NIR-IIb window (Fig. S1). Compared to the previously widely used HiPCO SWNTs, LV nanotubes exhibit higher fluorescence brightness in 1500-1700 nm region due to the smaller band-gaps and larger average diameter (Fig. S2).<sup>[4b]</sup> The LV SWNTs grown at 950 °C were then suspended by sonication and sorted through a chromatography column to enrich semiconducting SWNTs (See Experimental Details in SI)<sup>[2j, 8]</sup>. Compared to raw material, the resulting semiconducting LV SWNTs exhibited enhanced semiconducting S<sub>11</sub>/S<sub>22</sub> (700-1800 nm) peaks and reduced metallic M<sub>11</sub> peaks (500-700 nm) in the UV-Vis-NIR absorption spectra (Fig. 1c), indicating successful enrichment of semiconducting LV SWNTs needed for biological imaging with bright fluorescence in the 1500-1700 nm range (Fig. 1b & Fig. 1d). The quantum yield of the sorted semiconducting LV SWNTs was measured to be  $\sim$  0.1% against a conventional calibration dye IR26 under an excitation of 808 nm (Fig. S3),<sup>[9]</sup> which was low but found sufficient for *in vivo* biological imaging in NIR-IIb region owing to the ultra-low background signal in this window.

The 1500-1700 nm emitting semiconducting LV SWNTs were then made stably suspended in aqueous biological solutions with highly biocompatible surface coating by employing an exchange functionalization method (see Experimental Details).<sup>[2g]</sup> To compare *in vivo* fluorescence imaging of mouse blood vessels in the hindlimb and brain (with intact scalp without craniotomy) in traditional NIR-I (850-900 nm), NIR-II (1000-1700 nm) and NIR-IIb (1500-1700 nm) regions, we intravenously injected indocyanine green (ICG) or a mixture of exchange-functionalized HiPCO and semiconducting LV SWNT into mouse tail vein. Due to

scattering of short wavelength photons by mouse tissues, images of mouse hindlimb acquired with ICG in the NIR-I window near ~850 nm were blurry and featureless (Fig. 2a). Imaging in the entire 1000-1700 nm NIR-II region was able to resolve vessel structures (Fig. 2b), but the sharpest images were only obtained in the 1500-1700 nm NIR-IIb window (Fig. 2c), owing to the minimization of scattered photons travelling through the skin, muscle and other tissues of mice by rejecting shorter wavelength photons < 1500 nm.

Non-invasive fluorescence cerebrovascular imaging of mouse brain vessels through intact scalp and skull was readily achieved with C57B1/6 mice at depths up to ~3 mm in the mouse cerebrovasculature after shaving to remove hair (Fig. 2d-f). Quantitatively, we measured the signal-to-background ratios (SBRs) for images recorded in various wavelength regions by plotting the cross-sectional intensity profiles of the same vessel imaged in NIR-I, NIR-II and NIR-IIb windows respectively (Fig. 2g-i). The SBR of the feature imaged in NIR-IIb was found to be higher than imaged in NIR-I and NIR-II (4.50 in NIR-IIb vs 2.01 in NIR-II and 1.19 in NIR-I), suggesting reduced tissue scattering can significantly lower the background signals for *in vivo* fluorescence imaging.

Next we performed high-magnification microscopic vessel imaging in both mice hindlimb and brain with a pixel size of 2.5  $\mu\text{m}$  in the NIR-IIb region and a shorter wavelength NIR-IIa region (1300-1400 nm, Fig. 1a)<sup>[2a]</sup>. By measuring Gaussian-fitted full width at half maximum (FWHM) of the cross-sectional intensity profiles of features, we found the width of the same hindlimb blood vessel imaged at a depth of ~3 mm in NIR-IIa (marked by a green line, Fig. 3a) and NIR-IIb (marked by a green line, Fig. 3b) was 9.7  $\mu\text{m}$  and 6.3  $\mu\text{m}$  respectively, suggesting an improved spatial resolution in the longer NIR-IIb window (Fig. 3c). Moreover, we evaluated the SBRs of a blood vessel (marked by white lines, Fig. 3a-b) in both imaging windows. A higher SBR of 3.85 was obtained in NIR-IIb compared to 1.56 in NIR-IIa for the same blood vessel due to reduced light scattering (Fig. 3d). The smallest vessel resolved by NIR-IIb fluorescence imaging in the mouse hindlimb was down to ~3.7  $\mu\text{m}$  at a depth of ~2.6 mm (Fig. 3e-f).

We also compared high-magnification cerebrovascular imaging in NIR-IIa<sup>[2a]</sup> and NIR-IIb regions. Compared to the NIR-IIa region, many vessels imaged in NIR-IIb showed generally improved spatial resolution (Fig. 3i, 5.40  $\mu\text{m}$  in NIR-IIb vs 9.42  $\mu\text{m}$  in NIR-IIa for the same

blood vessel, marked by green lines in Fig. 3g-h) and increased SBR (Fig. 3j, 7.44 in NIR-IIb vs 4.91 in NIR-IIa for the same vessel, marked by white lines in Fig. 3g-h). A small vessel with a width down to 4.0  $\mu\text{m}$  was measured in NIR-IIb region at a depth of  $\sim 2.8$  mm below the intact scalp and skull, achieving microns scale resolution for *in vivo* fluorescence brain imaging at  $> 2$  mm depth (Fig. 3k-l). This was the first time  $< 5$  micron resolution was achieved for fluorescence imaging at such depth *in vivo*. Previous fluorescence brain imaging has generally relied on invasive craniotomy with a penetration depth limited to  $\sim 1.6$  mm using various techniques including two-photon microscopy.<sup>[10]</sup> Note that imaging depth was determined through this work by recording the vertical axis travel distance of the microscopic objective with the surface of the skin set to be depth zero.

To perform video-rate fluorescence imaging of blood vessels in the mouse hindlimb in the NIR-IIb region, we injected a 200  $\mu\text{L}$  solution of exchanged semiconducting LV SWNTs into the tail vein of an athymic nude mouse and performed NIR-IIb fluorescence imaging at a speed of 4.6 frames/second using a 2D InGaAs camera (Princeton Instruments, quantum efficiency curve up to 1700 nm shown in Fig. S6) under the excitation of an 808-nm laser diode (Supplementary Movie 1). Blood flow into the femoral artery was clearly observed upon injection by video-rate imaging (Fig. 4a). In addition to the main femoral artery, real-time blood flow into numerous smaller high-order arterial vessel branches was also observed (See Fig. 4b-c and Movie 1). These smaller vessels appeared deeper in the body than the femoral artery and were not resolvable by imaging in the 1000-1400 nm range.<sup>[2b]</sup> Blood flow speeds in various arterial vessels were quantified from video imaging (Movie 1) by plotting the distance travelled by the signal front vs. time (Fig. S4),<sup>[2b]</sup> affording a spatially resolved blood flow map (Fig. 4f) showing blood flow speeds of  $\sim 22.6$  mm/s in the femoral artery and 1.1 to 4.8 mm/s in the smaller arterial branches. To our knowledge, this was the first time that blood flow velocities (over a broad range of 1-20 mm/s) in multiple vessels of mice were mapped out simultaneously. Blood flow velocimetry over such a broad dynamic range from  $\sim 1$  mm/s to  $>20$  mm/s with spatially resolved individual vessels has not been achievable with other standard techniques such as laser Doppler and ultrasonography, owing to the poor spatial resolution, speckle artifacts and small dynamic range.<sup>[2b, 3, 11]</sup>

The femoral veins were observed at ~26 s post injection (p.i.) (Fig. 4e), as these vessel structures became fluorescent in NIR-IIb due to blood flow completing a systemic circulation cycle in the hindlimb. Principal component analysis (PCA) of the video-rate image frames was performed to group the image pixels with similar time variance into distinct components, clearly identifying the various arterial branches and differentiating them from the venous vessels (Fig. 4f).<sup>[2h, 12]</sup> Qualitatively, the NIR-IIb images (Fig. 4a-e) and video (Supplementary Movie 1) were some of the sharpest and lowest noise/background optical images of mouse hindlimb vessels recorded in the > 1000 nm NIR region.

Lastly, we explored the NIR-IIb emitting SWNTs for *in vivo* tumor imaging. By intravenously injecting exchanged semiconducting LV SWNTs into a balb/c mouse bearing two subcutaneous 4T1 murine breast tumors, we performed video-rate (4.6 frames/second) NIR-IIb fluorescence imaging of the mouse under an 808 nm excitation (Supplementary Movie 2). Due to pulmonary circulation, an intensity spike in the lung (a deep organ in mouse) was clearly resolved post injection into the tail-vein (Fig. 5a-b). Following the lung, NIR-IIb signals in major organs in the systemic circulation such as kidneys were clearly observed (Fig. 5c-d). The vascular structures surrounding the tumors started to appear in a prominent manner at ~3.9 s p.i. (Fig. 5d-e). These deep vessels were hard to resolve by imaging in shorter wavelength regions due to scattering by muscles and other tissues atop. Registration of the inner organs and vessels was evident by applying PCA to the frames of the video-rate movie (Fig. 5f).

Over a SWNT blood circulation half-life time of ~ 5 hours,<sup>[13]</sup> the nanotubes gradually accumulated within the tumors owing to the enhanced permeability and retention (EPR) effect.<sup>[2i, 14]</sup> High-magnification microscopic NIR-IIb fluorescence imaging inside the left tumor was performed using a 50X objective (with a pixel size of 0.5  $\mu\text{m}$ ) at ~ 96 hours p.i.. At an imaging depth of ~1 mm inside the tumor under the skin, we performed excitation-polarization dependent imaging and resolved individual nanotubes within the tumor. By linearly polarizing the 808 nm excitation light at various angles, a 180° periodic modulation of SWNT emission was observed due to the absorption/emission polarization dependence along the tube axis (Fig. 5g-i & Supplementary Movie 3, the individual nanotube whose intensity change was shown in Fig. 5i was marked by a white arrow in Fig. 5g-h).<sup>[15]</sup> As a result, the minimal and maximal fluorescence intensities of the individual nanotube were observed when the excitation light was

polarized perpendicular to (Fig. 5g) and along (Fig. 5h) the tube axis respectively. Previously, single nanotube molecular imaging was only achieved on solid substrates<sup>[16]</sup> or solutions<sup>[15a]</sup>. Our result here demonstrated the possibility of single nanotube imaging at millimeters depths in the NIR-IIb window inside mice or other living biological systems, which could facilitate interrogating complex biological processes at molecular level *in vivo*.

We have shown that the long NIR imaging window of 1500-1700 nm is advantageous in minimizing photon scattering for *in vivo* fluorescence imaging. Water absorption is slightly higher in NIR-IIb than the traditional NIR window, but the absorption effect can be easily overcome with sufficiently bright fluorophores. This is an approach worth taking since scattering problems could not be easily solved or avoided unless longer wavelength photons are detected. NIR-IIb imaging offers the lowest light scattering among all NIR sub-regions that have been explored for *in vivo* fluorescence imaging thus far, affording unprecedented spatial resolution, imaging depth and high signal/background ratio for *in vivo* biological imaging. With NIR-IIb imaging, we succeeded single fluorophore imaging *in vivo* deep inside live biological systems. The results here are not limited to nanotube fluorophores, and can be generalized to other agents emitting in the up to 1700 nm region, hopefully with much higher quantum yield and more favorable pharmacokinetics, thus leading to potential clinical translation of NIR-II imaging.

## Acknowledgments

This study was supported by grants from National Institutes of Health-National Cancer Institute (NIH-NCI) No. 5R01CA135109-02 to H.D. LV SWNTs synthesis was performed at NREL, and was supported by the Solar Photochemistry Program, Division of Chemical Sciences, Geosciences, and Biosciences, Office of Basic Energy Sciences, U.S. Department of Energy (DOE), Grant DE-AC36-08GO28308 (for developing carbon nanomaterial with advanced properties and spectroscopic characterizations).

## References

[1] a)J. V. Frangioni, *Current Opinion in Chemical Biology* **2003**, *7*, 626; b)S. A. Hilderbrand, R. Weissleder, *Current opinion in chemical biology* **2010**, *14*, 71; c)X. Le Guével, C. Spies, N. Daum,

G. Jung, M. Schneider, *Nano Research* **2012**, *5*, 379; d) T. Yang, Q. Liu, S. Pu, Z. Dong, C. Huang, F. Li, *Nano Research* **2012**, *5*, 494.

[2] a) G. Hong, S. Diao, J. Chang, A. L. Antaris, C. Chen, B. Zhang, S. Zhao, D. N. Atochin, P. L. Huang, K. I. Andreasson, *Nature Photonics* **2014**; b) G. Hong, J. C. Lee, J. T. Robinson, U. Raaz, L. Xie, N. F. Huang, J. P. Cooke, H. Dai, *Nature medicine* **2012**; c) G. Hong, Y. Zou, A. L. Antaris, S. Diao, D. Wu, K. Cheng, X. Zhang, C. Chen, B. Liu, Y. He, *Nature Communications* **2014**, *5*; d) D. Naczynski, M. Tan, M. Zevon, B. Wall, J. Kohl, A. Kulesa, S. Chen, C. Roth, R. Rimani, P. Moghe, *Nature communications* **2013**, *4*; e) A. M. Smith, M. C. Mancini, S. Nie, *Nature nanotechnology* **2009**, *4*, 710; f) Z. Tao, G. Hong, C. Shinji, C. Chen, S. Diao, A. L. Antaris, B. Zhang, Y. Zou, H. Dai, *Angewandte Chemie* **2013**; g) K. Welsher, Z. Liu, S. P. Sherlock, J. T. Robinson, Z. Chen, D. Daranciang, H. Dai, *Nature nanotechnology* **2009**, *4*, 773; h) K. Welsher, S. P. Sherlock, H. J. Dai, *Proceedings of the National Academy of Sciences of the United States of America* **2011**, *108*, 8943; i) H. Yi, D. Ghosh, M.-H. Ham, J. Qi, P. W. Barone, M. S. Strano, A. M. Belcher, *Nano letters* **2012**, *12*, 1176; j) S. Diao, G. Hong, J. T. Robinson, L. Jiao, A. L. Antaris, J. Z. Wu, C. L. Choi, H. Dai, *Journal of the American Chemical Society* **2012**, *134*, 16971; k) G. Hong, J. T. Robinson, Y. Zhang, S. Diao, A. L. Antaris, Q. Wang, H. Dai, *Angewandte Chemie* **2012**, *124*, 9956; l) J. T. Robinson, G. Hong, Y. Liang, B. Zhang, O. K. Yaghi, H. Dai, *Journal of the American Chemical Society* **2012**, *134*, 10664.

[3] G. Hong, J. C. Lee, A. Jha, S. Diao, K. H. Nakayama, L. Hou, T. C. Doyle, J. T. Robinson, A. L. Antaris, H. Dai, *Circulation: Cardiovascular Imaging* **2014**, *7*, 517.

[4] a) T. Guo, P. Nikolaev, A. Thess, D. Colbert, R. Smalley, *Chemical Physics Letters* **1995**, *243*, 49; b) S. M. Bachilo, M. S. Strano, C. Kittrell, R. H. Hauge, R. E. Smalley, R. B. Weisman, *Science* **2002**, *298*, 2361; c) M. J. O'connell, S. M. Bachilo, C. B. Huffman, V. C. Moore, M. S. Strano, E. H. Haroz, K. L. Rialon, P. J. Boul, W. H. Noon, C. Kittrell, *Science* **2002**, *297*, 593.

[5] a) S. Lebedkin, K. Arnold, F. Hennrich, R. Krupke, B. Renker, M. M. Kappes, *New Journal of Physics* **2003**, *5*, 140; b) S. Lebedkin, F. Hennrich, T. Skipa, M. M. Kappes, *The Journal of Physical Chemistry B* **2003**, *107*, 1949; c) H. Zhao, S. Mazumdar, *Physical review letters* **2004**, *93*, 157402.

[6] A. Bashkatov, E. Genina, V. Kochubey, V. Tuchin, *Journal of Physics D: Applied Physics* **2005**, *38*, 2543.

[7] K. S. Mistry, B. A. Larsen, J. L. Blackburn, *ACS nano* **2013**, *7*, 2231.

[8] Y. Miyata, K. Shiozawa, Y. Asada, Y. Ohno, R. Kitaura, T. Mizutani, H. Shinohara, *Nano Research* **2011**, *4*, 963.

[9] J. E. Murphy, M. C. Beard, A. G. Norman, S. P. Ahrenkiel, J. C. Johnson, P. Yu, O. I. Micic, R. J. Ellingson, A. J. Nozik, *Journal of the American Chemical Society* **2006**, *128*, 3241.

[10] a) N. G. Horton, K. Wang, D. Kobat, C. G. Clark, F. W. Wise, C. B. Schaffer, C. Xu, *Nature Photonics* **2013**, *7*, 205; b) D. Kobat, N. G. Horton, C. Xu, *Journal of biomedical optics* **2011**, *16*, 106014; c) P. Theer, M. T. Hasan, W. Denk, *Optics letters* **2003**, *28*, 1022.

[11] a) J. W. Xuan, M. Bygrave, H. Jiang, F. Valiyeva, J. Dunmore-Buyze, D. W. Holdsworth, J. I. Izawa, G. Bauman, M. Moussa, S. F. Winter, *Cancer Research* **2007**, *67*, 2830; b) K. Z. Abd-Elmoniem, A. Youssef, Y. M. Kadah, *Biomedical Engineering, IEEE Transactions on* **2002**, *49*, 997.

[12] E. M. Hillman, A. Moore, *Nature photonics* **2007**, *1*, 526.

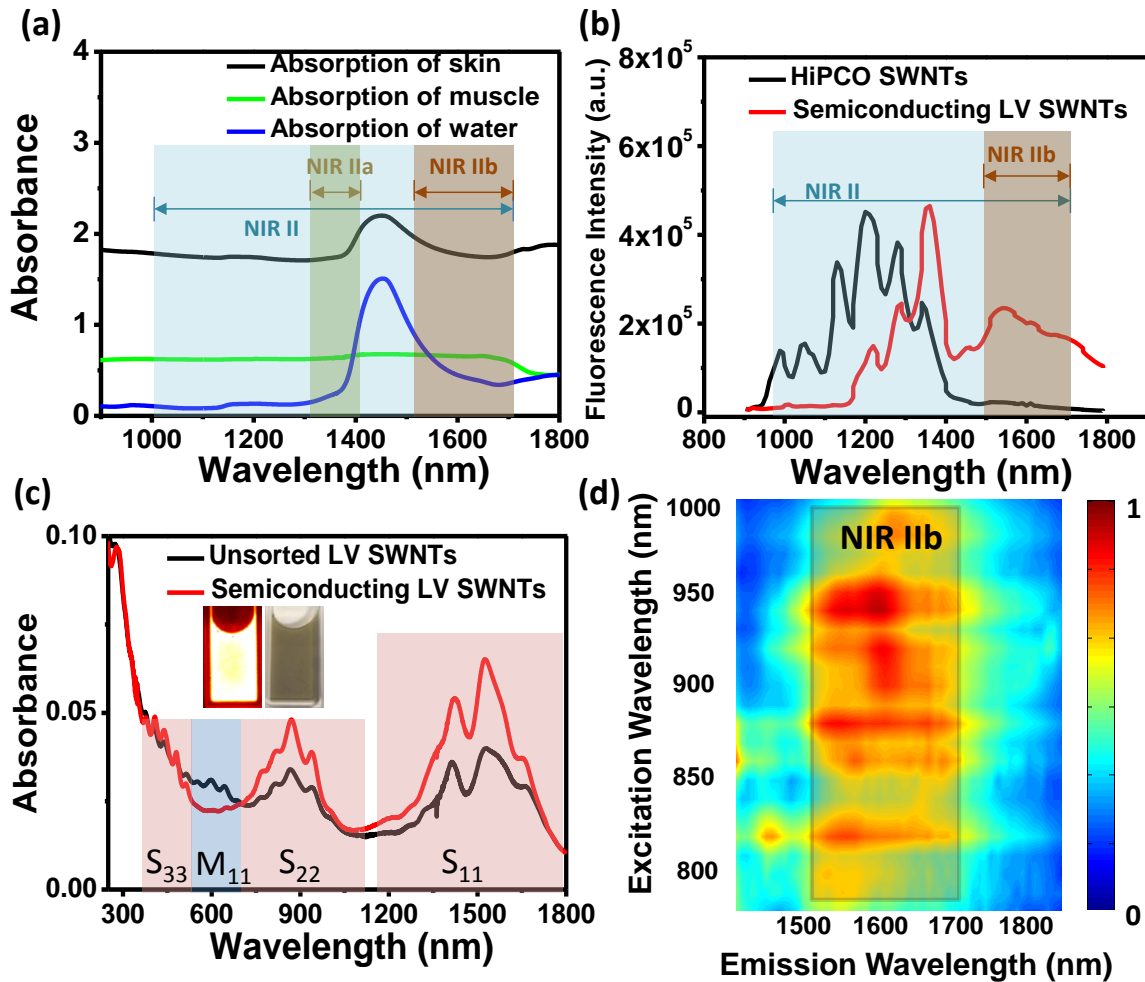
[13] Z. Liu, C. Davis, W. Cai, L. He, X. Chen, H. Dai, *Proceedings of the National Academy of Sciences* **2008**, *105*, 1410.

[14] A. K. Iyer, G. Khaled, J. Fang, H. Maeda, *Drug discovery today* **2006**, *11*, 812.

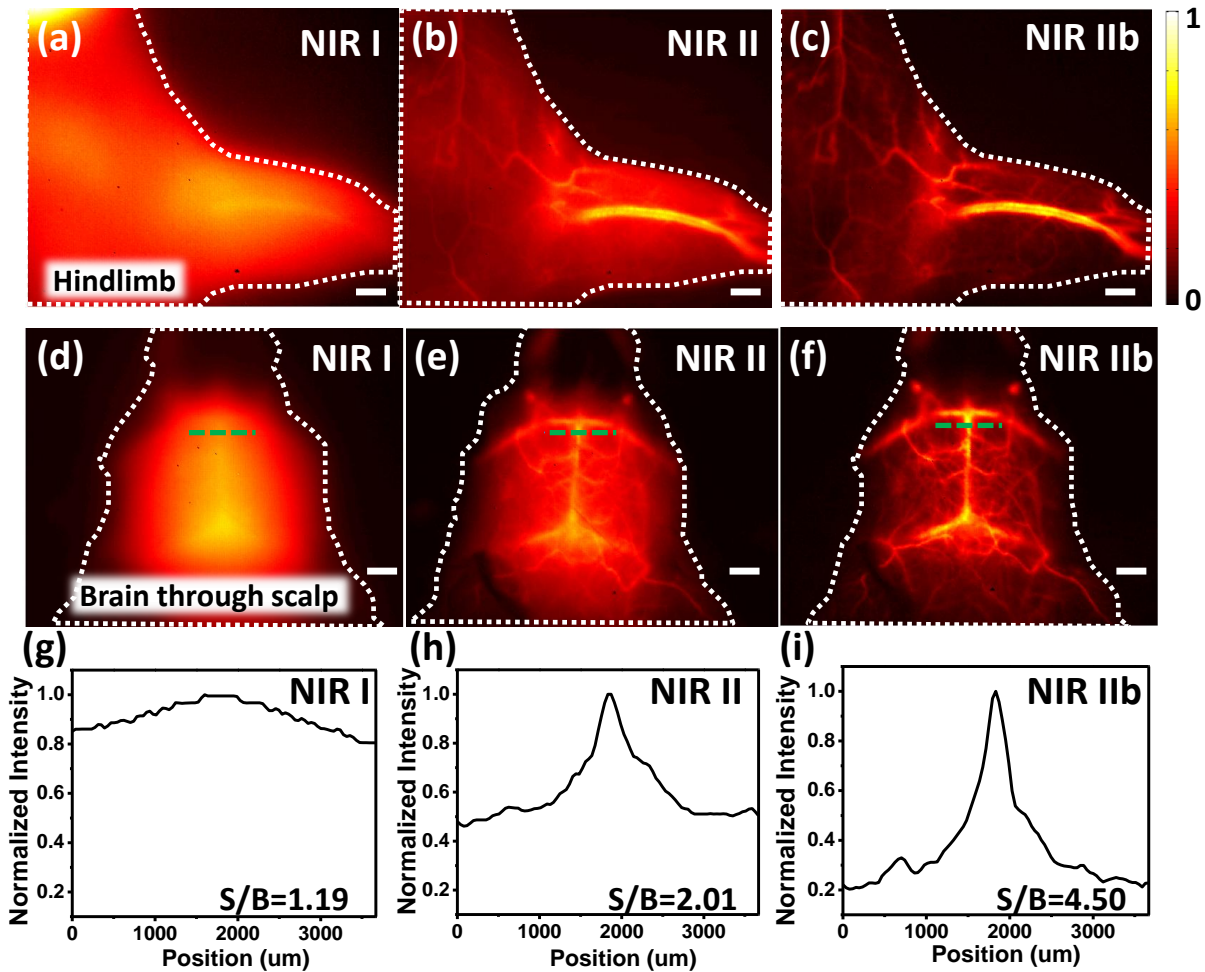
[15] a) G. Hong, J. Z. Wu, J. T. Robinson, H. Wang, B. Zhang, H. Dai, *Nature communications* **2012**, *3*, 700; b) D. A. Tsyboulski, S. M. Bachilo, R. B. Weisman, *Nano letters* **2005**, *5*, 975.

[16] G. Hong, S. M. Tabakman, K. Welsher, H. Wang, X. Wang, H. Dai, *Journal of the American Chemical Society* **2010**, *132*, 15920.

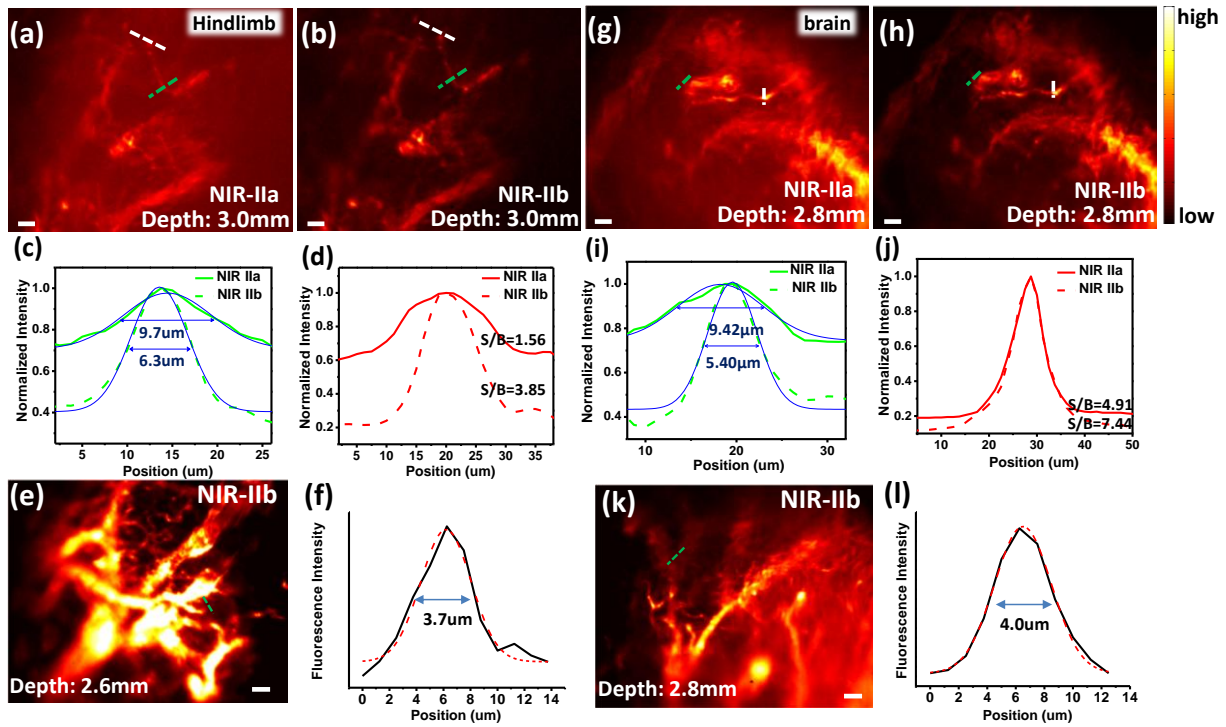
## Figures



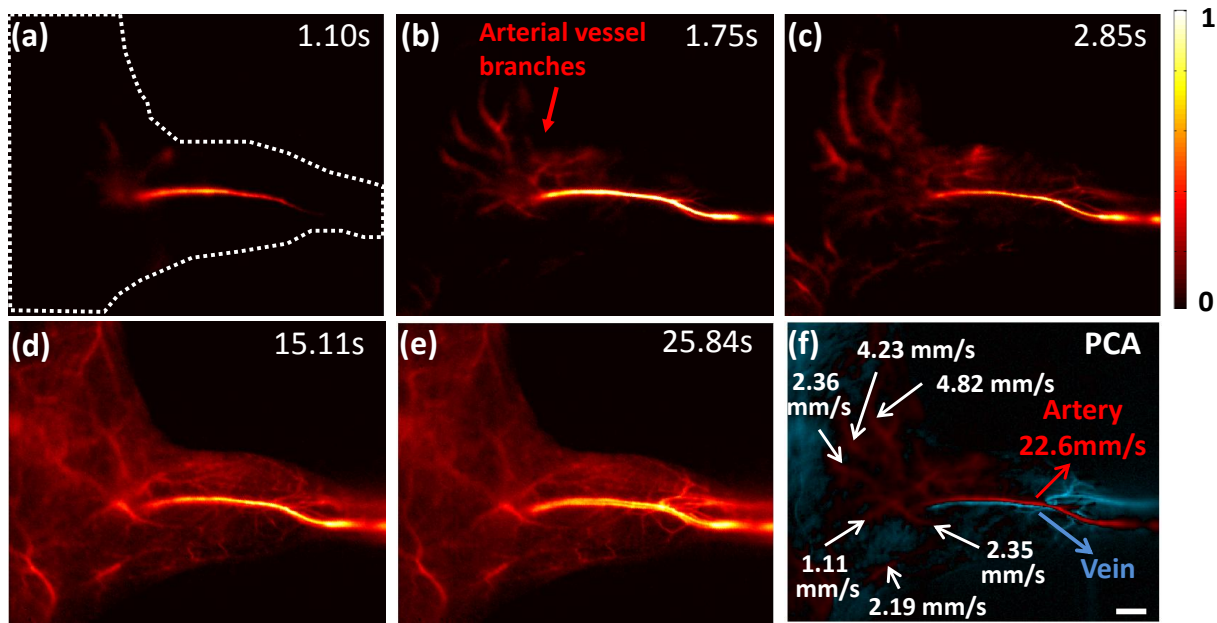
**Figure 1.** Semiconducting laser vaporization (LV) SWNTs for fluorescence imaging in NIR-IIb region. **a)** Optical absorption spectra of water, mouse skin and mouse muscle in the range of 900-1800 nm. NIR-II (1000-1700 nm), NIR-IIa (1300-1400 nm) and NIR-IIb (1500-1700 nm) regions are labeled in distinct colors. **b)** NIR fluorescence spectra of HiPCO SWNTs and semiconducting LV SWNTs upon the excitation of an 808 nm fiber-coupled diode laser. **c)** Optical absorption spectra of pristine LV SWNTs and separated semiconducting LV SWNTs. Photoluminescence (inset, left) and optical (inset, right) images of semiconducting LV SWNTs are also shown. **d)** The photoluminescence versus excitation (PLE) map of semiconducting LV SWNTs showing bright emission in the NIR-IIb region.



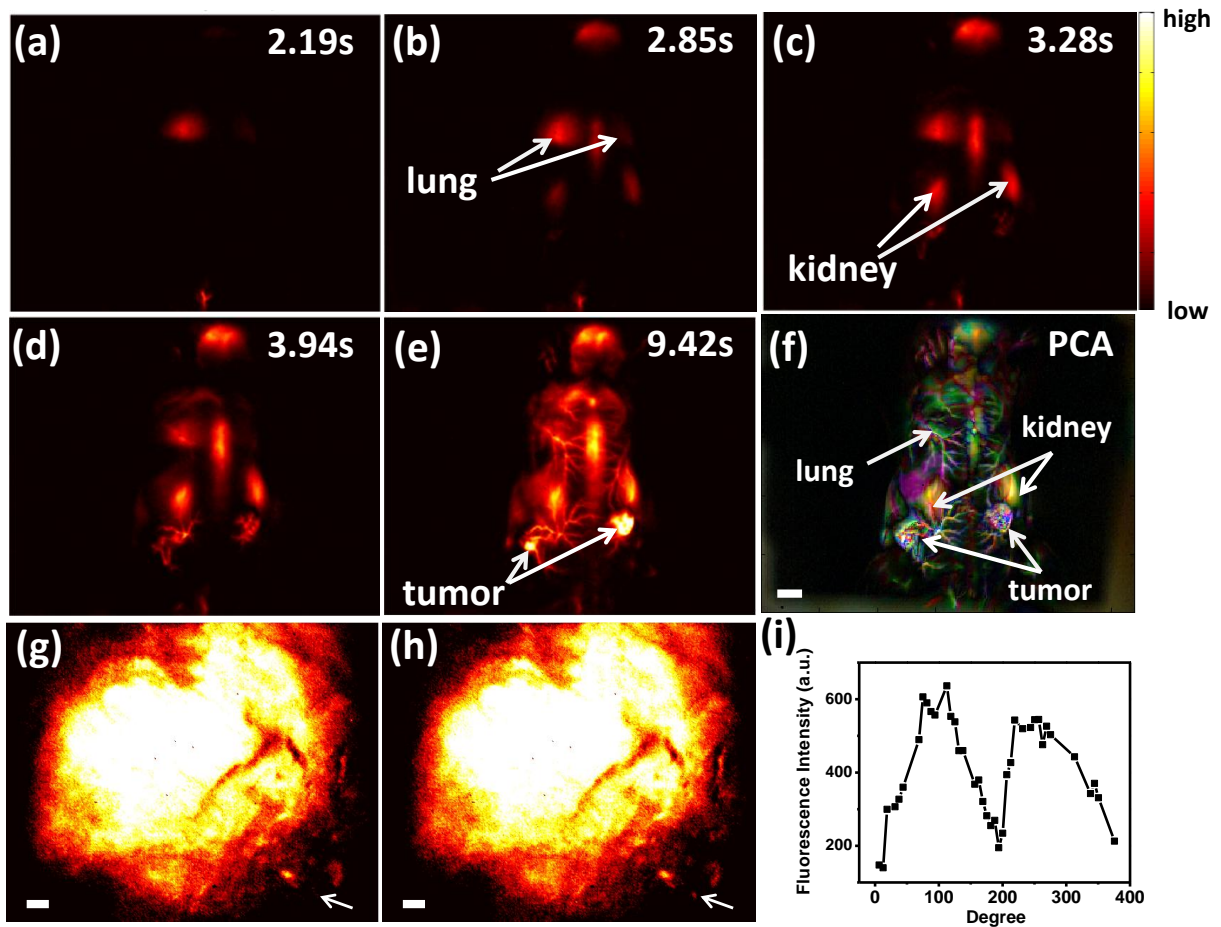
**Figure 2.** Comparison of fluorescence images of mouse hindlimb and brain in various NIR regions. **a)-c)** Fluorescence images of an athymic nude mouse hindlimb in NIR-I, NIR-II and NIR-IIb regions after injecting ICG or exchanged HiPCO/semiconducting LV SWNTs as emitters. **d)-f)** Mouse cerebrovascular fluorescence images without craniotomy in NIR-I, NIR-II and NIR-IIb regions of a C57B1/6 mouse by injecting ICG or exchanged HiPCO/semiconducting LV SWNTs (with hair on the scalp removed). **g)-i)** Signal-to-background ratio (SBR) analysis of NIR-I, NIR-II and NIR-IIb images by plotting the cross-sectional intensity profiles of the same blood vessel. The SBR is found to be 1.19 in NIR-I, 2.01 in NIR-II and 4.50 in NIR-IIb regions. The scale bars in **a-f** indicate 2 mm.



**Figure 3.** High-magnification vessel imaging in mouse hindlimb and brain in NIR-IIa (1300-1400 nm) and IIb (1500-1700 nm) windows. **a)-b)** High-magnification microscopic images of mouse hindlimb vessels at an imaging focal depth of 3 mm taken in NIR-IIa and NIR-IIb windows. **c)** Cross-sectional intensity profiles of a small hindlimb vessel (marked by green lines in a&b). **d)** The signal-to-background ratio (SBR) analysis of a blood vessel (marked by white lines in a&b) in NIR-IIa and NIR-IIb. The background signals were evaluated by averaging the baseline signals in the cross-sectional intensity profiles. **e)-f)** A small blood vessel with a width of 3.7  $\mu$ m in the hindlimb resolved in NIR-IIb at an imaging depth of 2.6 mm. **g)-h)** High-magnification cerebrovascular image in NIR-IIa and NIR-IIb regions. **i)** A small blood vessel was found to be 9.42  $\mu$ m wide in NIR-IIa and 5.40  $\mu$ m wide in NIR-IIb by Gaussian-fitted FWHM (marked by green lines in g&h). **j)** The SBR of a vessel (marked by white lines in g&h) was measured to be 4.91 in NIR-IIa and 7.44 in NIR-IIb. **k)-l)** A NIR-IIb fluorescence cerebrovascular image resolving a small vessel (marked by a green line in k) of a width of ~ 4.0  $\mu$ m at an imaging depth of ~ 2.8 mm. All the scale bars indicate 40  $\mu$ m.

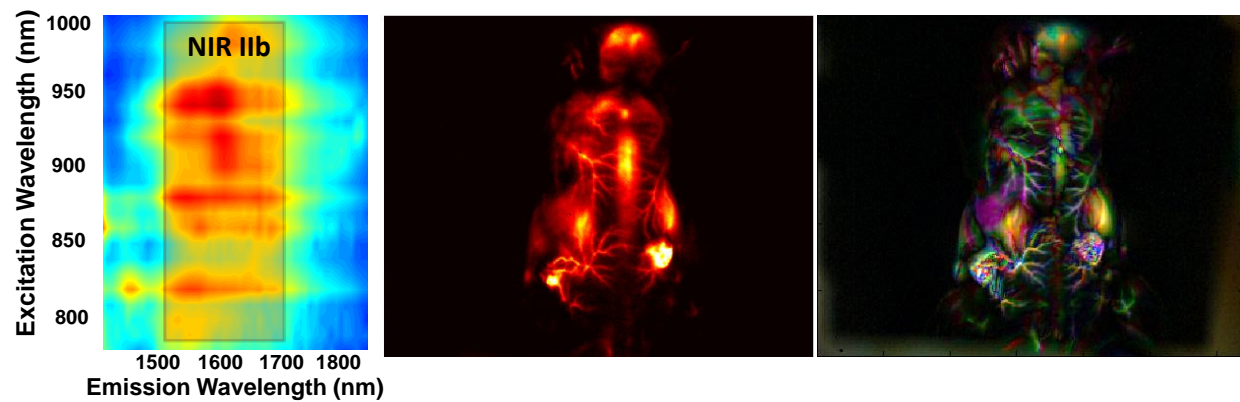


**Figure 4.** NIR-IIb fluorescence imaging of mouse hindlimb vessels and dynamic contrast-based vessel type differentiation. **a)-e)** Time course NIR-IIb fluorescence images after intravenous injection of semiconducting LV SWNTs into the tail vein of an athymic nude mouse. **f)** PCA overlaid image showing the differentiation of arterial (color-coded in red) and venous (color-coded in blue) vessels. The blood flow velocities in femoral artery and small, higher-order arterial vessels are labeled in **f**. The scale bar indicates 2 mm.



**Figure 5.** *In vivo* video-rate NIR-IIb tumor imaging in live mouse and non-invasive single fluorophore imaging inside tumor. **a)-e)** Time course NIR-IIb fluorescence images of the tumor-bearing mice after intravenous injection of exchanged semiconducting LV SWNTs with a video rate of 4.6 frames/second. **f)** Overlaid PCA image of the early image frames differentiating inner organs and vascular structures surrounding tumors. **g)-i)** Single fluorophore imaging inside left tumor by recording the 180° periodic modulation of SWNT (indicated by white arrows in g-h) intensity change when polarizing the excitation light, with an imaging depth of ~1mm. The scale bar in **f** indicate 4 mm, the scale bars in **g&h** indicate 10  $\mu$ m.

## TOC graphic



Keywords: fluorescence; nanotechnology; imaging agents; cancer; near-infrared